Eur. Phys. J. C (2009) 63: 611–623
DOI 10.1140/epjc/s10052-009-1123-y

THE EUROPEAN PHYSICAL JOURNAL C

Regular Article - Experimental Physics

Correlations between polarisation states of W particles in the reaction $e^-e^+ \to W^-W^+$ at LEP2 energies 189–209 GeV

The DELPHI Collaboration

J. Abdallah[27], P. Abreu[24], W. Adam[56], P. Adzic[13], T. Albrecht[19], R. Alemany-Fernandez[10], T. Allmendinger[19], P.P. Allport[25], U. Amaldi[31], N. Amapane[49], S. Amato[53], E. Anashkin[38], A. Andreazza[30], S. Andringa[24], N. Anjos[24], P. Antilogus[27], W-D. Apel[19], Y. Arnoud[16], S. Ask[10], B. Asman[48], J.E. Augustin[27], A. Augustinus[10], P. Baillon[10], A. Ballestrero[50], P. Bambade[22], R. Barbier[29], D. Bardin[18], G.J. Barker[58], A. Baroncelli[41], M. Battaglia[10], M. Baubillier[27], K-H. Becks[59], M. Begalli[8], A. Behrmann[59], E. Ben-Haim[22], N. Benekos[34], A. Benvenuti[6], C. Berat[16], M. Berggren[27], D. Bertrand[3], M. Besancon[42], N. Besson[42], D. Bloch[11], M. Blom[33], M. Bluj[57], M. Bonesini[31], M. Boonekamp[42], P.S.L. Booth[25,a], G. Borisov[23], O. Botner[54], B. Bouquet[22], T.J.V. Bowcock[25], I. Boyko[18], M. Bracko[45], R. Brenner[54], E. Brodet[37], P. Bruckman[20], J.M. Brunet[9], B. Buschbeck[56], P. Buschmann[59], M. Calvi[31], T. Camporesi[10], V. Canale[40], F. Carena[10], N. Castro[24], F. Cavallo[6], M. Chapkin[44], Ph. Charpentier[10], P. Checchia[38], R. Chierici[10], P. Chliapnikov[44], J. Chudoba[10], S.U. Chung[10], K. Cieslik[20], P. Collins[10], R. Contri[15], G. Cosme[22], F. Cossutti[51], M.J. Costa[55], D. Crennell[39], J. Cuevas[36], J. D'Hondt[3], T. da Silva[53], W. Da Silva[27], G. Della Ricca[51], A. De Angelis[52], W. De Boer[19], C. De Clercq[3], B. De Lotto[52], N. De Maria[49], A. De Min[38], L. de Paula[53], L. Di Ciaccio[40], A. Di Simone[41], K. Doroba[57], J. Drees[59,10], G. Eigen[5], T. Ekelof[54], M. Ellert[54], M. Elsing[10], M.C. Espirito Santo[24], G. Fanourakis[13], D. Fassouliotis[13,4], M. Feindt[19], J. Fernandez[43], A. Ferrer[55], F. Ferro[15], U. Flagmeyer[59], H. Foeth[10], E. Fokitis[34], F. Fulda-Quenzer[22], J. Fuster[55], M. Gandelman[53], C. Garcia[55], Ph. Gavillet[10], E. Gazis[34], R. Gokieli[10,57], B. Golob[45,47], G. Gomez-Ceballos[43], P. Goncalves[24], E. Graziani[41], G. Grosdidier[22], K. Grzelak[57], J. Guy[39], C. Haag[19], A. Hallgren[54], K. Hamacher[59], K. Hamilton[37], S. Haug[35], F. Hauler[19], V. Hedberg[28], M. Hennecke[19], J. Hoffman[57], S-O. Holmgren[48], P.J. Holt[10], M.A. Houlden[25], J.N. Jackson[25], G. Jarlskog[28], P. Jarry[42], D. Jeans[37], E.K. Johansson[48], P. Jonsson[29], C. Joram[10], L. Jungermann[19], F. Kapusta[27], S. Katsanevas[29], E. Katsoufis[34], G. Kernel[45], B.P. Kersevan[45,47], U. Kerzel[19], B.T. King[25], N.J. Kjaer[10], P. Kluit[33], P. Kokkinias[13], C. Kourkoumelis[4], O. Kouznetsov[18], Z. Krumstein[18], M. Kucharczyk[20], J. Lamsa[1], G. Leder[56], F. Ledroit[16], L. Leinonen[48], R. Leitner[32], J. Lemonne[3], V. Lepeltier[22,a], T. Lesiak[20], W. Liebig[59], D. Liko[56], A. Lipniacka[48], J.H. Lopes[53], J.M. Lopez[36], D. Loukas[13], P. Lutz[42], L. Lyons[37], J. MacNaughton[56], A. Malek[59], S. Maltezos[34], F. Mandl[56], J. Marco[43], R. Marco[43], B. Marechal[53], M. Margoni[38], J-C. Marin[10], C. Mariotti[10], A. Markou[13], C. Martinez-Rivero[43], J. Masik[14], N. Mastroyiannopoulos[13], F. Matorras[43], C. Matteuzzi[31], F. Mazzucato[38], M. Mazzucato[38], R. Mc Nulty[25], C. Meroni[30], E. Migliore[49], W. Mitaroff[56], U. Mjoernmark[28], T. Moa[48], M. Moch[19], K. Moenig[10,12], R. Monge[15], J. Montenegro[33], D. Moraes[53], S. Moreno[24], P. Morettini[15], U. Mueller[59], K. Muenich[59], M. Mulders[33], L. Mundim[8], W. Murray[39], B. Muryn[21], G. Myatt[37], T. Myklebust[35], M. Nassiakou[13], F. Navarria[6], K. Nawrocki[57], S. Nemecek[14], R. Nicolaidou[42], M. Nikolenko[18,11], A. Oblakowska-Mucha[21], V. Obraztsov[44], A. Olshevski[18], A. Onofre[24], R. Orava[17], K. Osterberg[17], A. Ouraou[42], A. Oyanguren[55], M. Paganoni[31], S. Paiano[6], J.P. Palacios[25], H. Palka[20], Th.D. Papadopoulou[34], L. Pape[10], C. Parkes[26], F. Parodi[15], U. Parzefall[10], A. Passeri[41], O. Passon[59], L. Peralta[24], V. Perepelitsa[55], A. Perrotta[6], A. Petrolini[15], J. Piedra[43], L. Pieri[41], F. Pierre[42], M. Pimenta[24], E. Piotto[10], T. Podobnik[45,47], V. Poireau[10], M.E. Pol[7], G. Polok[20], V. Pozdniakov[18], N. Pukhaeva[18], A. Pullia[31], D. Radojicic[37], P. Rebecchi[10], J. Rehn[19], D. Reid[33], R. Reinhardt[59], P. Renton[37], F. Richard[22], J. Ridky[14], M. Rivero[43], D. Rodriguez[43], A. Romero[49], P. Ronchese[38], P. Roudeau[22], T. Rovelli[6], V. Ruhlmann-Kleider[42], D. Ryabtchikov[44], A. Sadovsky[18], L. Salmi[17], J. Salt[55], C. Sander[19], A. Savoy-Navarro[27], U. Schwickerath[10], R. Sekulin[39], M. Siebel[59], A. Sisakian[18], G. Smadja[29], O. Smirnova[28], A. Sokolov[44], A. Sopczak[23], R. Sosnowski[57], T. Spassov[10], M. Stanitzki[19], A. Stocchi[22], J. Strauss[56], B. Stugu[5], M. Szczekowski[57], M. Szeptycka[57], T. Szumlak[21], T. Tabarelli[31], F. Tegenfeldt[54], J. Timmermans[33,b], L. Tkatchev[18], M. Tobin[25], S. Todorovova[14], B. Tome[24], A. Tonazzo[31], P. Tortosa[55], P. Travnicek[14], D. Treille[10], G. Tristram[9], M. Trochimczuk[57], C. Troncon[30], M-L. Turluer[42], I.A. Tyapkin[18], P. Tyapkin[18], S. Tzamarias[13], V. Uvarov[44], G. Valenti[6], P. Van Dam[33], J. Van Eldik[10], N. van Remortel[2], I. Van Vulpen[10], G. Vegni[30], F. Veloso[24], W. Venus[39], P. Verdier[29], V. Verzi[40], D. Vilanova[42], L. Vitale[51], V. Vrba[14], H. Wahlen[59], A.J. Washbrook[25],

C. Weiser[19], D. Wicke[10], J. Wickens[3], G. Wilkinson[37], M. Winter[11], M. Witek[20], O. Yushchenko[44], A. Zalewska[20], P. Zalewski[57], D. Zavrtanik[46], V. Zhuravlov[18], N.I. Zimin[18], A. Zintchenko[18], M. Zupan[13]

[1]Department of Physics and Astronomy, Iowa State University, Ames, IA 50011-3160, USA
[2]Physics Department, Universiteit Antwerpen, Universiteitsplein 1, 2610 Antwerpen, Belgium
[3]IIHE, ULB-VUB, Pleinlaan 2, 1050 Brussels, Belgium
[4]Physics Laboratory, University of Athens, Solonos Str. 104, 10680 Athens, Greece
[5]Department of Physics, University of Bergen, Allégaten 55, 5007 Bergen, Norway
[6]Dipartimento di Fisica, Università di Bologna and INFN, Viale C. Berti Pichat 6/2, 40127 Bologna, Italy
[7]Centro Brasileiro de Pesquisas Físicas, rua Xavier Sigaud 150, 22290 Rio de Janeiro, Brazil
[8]Inst. de Física, Univ. Estadual do Rio de Janeiro, rua São Francisco Xavier 524, Rio de Janeiro, Brazil
[9]Collège de France, Lab. de Physique Corpusculaire, IN2P3-CNRS, 75231 Paris Cedex 05, France
[10]CERN, 1211 Geneva 23, Switzerland
[11]Institut de Recherches Subatomiques, IN2P3–CNRS/ULP-BP20, 67037 Strasbourg Cedex, France
[12]DESY-Zeuthen, Platanenallee 6, 15735 Zeuthen, Germany
[13]Institute of Nuclear Physics, N.C.S.R. Demokritos, P.O. Box 60228, 15310 Athens, Greece
[14]FZU, Inst. of Phys. of the C.A.S. High Energy Physics Division, Na Slovance 2, 182 21, Praha 8, Czech Republic
[15]Dipartimento di Fisica, Università di Genova and INFN, Via Dodecaneso 33, 16146 Genova, Italy
[16]Institut des Sciences Nucléaires, IN2P3-CNRS, Université de Grenoble 1, 38026 Grenoble Cedex, France
[17]Helsinki Institute of Physics and Department of Physical Sciences, P.O. Box 64, 00014 University of Helsinki, Finland
[18]Joint Institute for Nuclear Research, Dubna, Head Post Office, P.O. Box 79, 101 000 Moscow, Russian Federation
[19]Institut für Experimentelle Kernphysik, Universität Karlsruhe, Postfach 6980, 76128 Karlsruhe, Germany
[20]Institute of Nuclear Physics PAN, Ul. Radzikowskiego 152, 31142 Krakow, Poland
[21]Faculty of Physics and Nuclear Techniques, University of Mining and Metallurgy, 30055 Krakow, Poland
[22]LAL, Univ Paris-Sud, CNRS/IN2P3, Orsay, France
[23]School of Physics and Chemistry, University of Lancaster, Lancaster LA1 4YB, UK
[24]LIP, IST, FCUL, Av. Elias Garcia, 14-1º, 1000 Lisboa Codex, Portugal
[25]Department of Physics, University of Liverpool, P.O. Box 147, Liverpool L69 3BX, UK
[26]Dept. of Physics and Astronomy, Kelvin Building, University of Glasgow, Glasgow G12 8QQ, UK
[27]LPNHE, IN2P3-CNRS, Univ. Paris VI et VII, Tour 33 (RdC), 4 place Jussieu, 75252 Paris Cedex 05, France
[28]Department of Physics, University of Lund, Sölvegatan 14, 223 63 Lund, Sweden
[29]Université Claude Bernard de Lyon, IPNL, IN2P3-CNRS, 69622 Villeurbanne Cedex, France
[30]Dipartimento di Fisica, Università di Milano and INFN-MILANO, Via Celoria 16, 20133 Milan, Italy
[31]Dipartimento di Fisica, Univ. di Milano-Bicocca and INFN-MILANO, Piazza della Scienza 3, 20126 Milan, Italy
[32]IPNP of MFF, Charles Univ., Areal MFF, V Holesovickach 2, 180 00, Praha 8, Czech Republic
[33]NIKHEF, Postbus 41882, 1009 DB Amsterdam, The Netherlands
[34]National Technical University, Physics Department, Zografou Campus, 15773 Athens, Greece
[35]Physics Department, University of Oslo, Blindern, 0316 Oslo, Norway
[36]Dpto. Fisica, Univ. Oviedo, Avda. Calvo Sotelo s/n, 33007 Oviedo, Spain
[37]Department of Physics, University of Oxford, Keble Road, Oxford OX1 3RH, UK
[38]Dipartimento di Fisica, Università di Padova and INFN, Via Marzolo 8, 35131 Padua, Italy
[39]Rutherford Appleton Laboratory, Chilton, Didcot OX11 OQX, UK
[40]Dipartimento di Fisica, Università di Roma II and INFN, Tor Vergata, 00173 Rome, Italy
[41]Dipartimento di Fisica, Università di Roma III and INFN, Via della Vasca Navale 84, 00146 Rome, Italy
[42]DAPNIA/Service de Physique des Particules, CEA-Saclay, 91191 Gif-sur-Yvette Cedex, France
[43]Instituto de Fisica de Cantabria (CSIC-UC), Avda. los Castros s/n, 39006 Santander, Spain
[44]Inst. for High Energy Physics, Serpukov P.O. Box 35, Protvino, Moscow Region, Russian Federation
[45]J. Stefan Institute, Jamova 39, 1000 Ljubljana, Slovenia
[46]Laboratory for Astroparticle Physics, University of Nova Gorica, Kostanjeviska 16a, 5000 Nova Gorica, Slovenia
[47]Department of Physics, University of Ljubljana, 1000 Ljubljana, Slovenia
[48]Fysikum, Stockholm University, Box 6730, 113 85 Stockholm, Sweden
[49]Dipartimento di Fisica Sperimentale, Università di Torino and INFN, Via P. Giuria 1, 10125 Turin, Italy
[50]INFN, Sezione di Torino and Dipartimento di Fisica Teorica, Università di Torino, Via Giuria 1, 10125 Turin, Italy
[51]Dipartimento di Fisica, Università di Trieste and INFN, Via A. Valerio 2, 34127 Trieste, Italy
[52]Istituto di Fisica, Università di Udine and INFN, 33100 Udine, Italy
[53]Univ. Federal do Rio de Janeiro, C.P. 68528 Cidade Univ., Ilha do Fundão, 21945-970 Rio de Janeiro, Brazil
[54]Department of Radiation Sciences, University of Uppsala, P.O. Box 535, 751 21 Uppsala, Sweden
[55]IFIC, Valencia-CSIC, and D.F.A.M.N., U. de Valencia, Avda. Dr. Moliner 50, 46100 Burjassot (Valencia), Spain
[56]Institut für Hochenergiephysik, Österr. Akad. d. Wissensch., Nikolsdorfergasse 18, 1050 Vienna, Austria
[57]Inst. Nuclear Studies and University of Warsaw, Ul. Hoza 69, 00681 Warsaw, Poland
[58]University of Warwick, Coventry CV4 7AL, UK
[59]Fachbereich Physik, University of Wuppertal, Postfach 100 127, 42097 Wuppertal, Germany

Received: 26 February 2009 / Revised: 14 June 2009 / Published online: 1 September 2009
© Springer-Verlag / Società Italiana di Fisica 2009

Abstract In a study of the reaction $e^-e^+\to W^-W^+$ with the DELPHI detector, the probabilities of the two W particles occurring in the joint polarisation states transverse–transverse (TT), longitudinal–transverse plus transverse–longitudinal (LT) and longitudinal–longitudinal (LL) have been determined using the final states $WW\to l\nu q\bar{q}$ ($l = e, \mu$). The two-particle joint polarisation probabilities, i.e. the spin density matrix elements ρ_{TT}, ρ_{LT}, ρ_{LL}, are measured as functions of the W^- production angle, θ_{W^-}, at an average reaction energy of 198.2 GeV. Averaged over all $\cos\theta_{W^-}$, the following joint probabilities are obtained:

$$\bar{\rho}_{TT} = (67 \pm 8)\%,$$

$$\bar{\rho}_{LT} = (30 \pm 8)\%,$$

$$\bar{\rho}_{LL} = (3 \pm 7)\%.$$

These results are in agreement with the Standard Model predictions of 63.0%, 28.9% and 8.1%, respectively. The related polarisation cross-sections σ_{TT}, σ_{LT} and σ_{LL} are also presented.

1 Introduction

In the study of the reaction $e^-e^+\to W^-W^+$ at LEP2, the DELPHI Collaboration [1] and other LEP experiments [2, 3] have established that on average ∼25% of W particles are longitudinally polarised, as predicted by the Standard Model. The present study measures the joint two-particle spin density matrix elements which give the probabilities that both Ws are transversely polarised (W_TW_T), both are longitudinally polarised (W_LW_L) or that one W is transversely polarised while the associated W is longitudinal ($W_TW_L + W_LW_T$). In what follows, these correlations will be referred to as TT, LL and LT, respectively. This is a more detailed test of the Standard Model prediction for the W polarisation than those previously published. Production of longitudinal Ws is of particular interest because they are associated with the breaking of the electroweak symmetry. This study tests the theoretical prediction of the correlations and in particular, the prediction that the correlation LL is suppressed relative to LT.

The previously published measurements of the spin-dependent correlations between the W particles in the reaction $e^-e^+\to W^-W^+$ are by the OPAL Collaboration [4] and by the L3 Collaboration [5]. OPAL evaluated the cross-sections σ_{TT}, σ_{LT} and σ_{LL} from their data at 189 GeV with a comparatively low statistics. Their results are in poor agreement with the Standard Model. L3 used the $WW\to l\nu q\bar{q}$ and $WW\to q\bar{q}\,q\bar{q}$ events from their full LEP2 data set to establish the correlation between the decay planes of the two Ws. The correlation was found to be consistent with the Standard Model prediction.

The analysis presented in this paper uses only the events in which one W decays into an electron plus a neutrino or a muon plus neutrino, while the other W decays into two hadron jets. These "semi-leptonic" events are kinematically well constrained and they offer the best available data for any detailed analysis of this reaction. The τ semi-leptonic events are excluded because the uncertainties in their identification cause problems in WW correlation measurements. The fully hadronic final state $WW\to q\bar{q}q\bar{q}$ is also excluded because of the uncertainties in jet reconstruction: the charges of the hadron jets cannot be well measured and the particles from the four jets tend to overlap in the space of the detector, resulting in uncertainties in associations between the Ws and the measured jets.

A complete description of the polarisation states of the produced W particles is given in terms of the two-particle joint spin density matrix $\rho_{\lambda_1\lambda_1'\lambda_2\lambda_2'}$, where λ_1 and λ_2 are the helicities of the W^- and W^+ respectively. In terms of the W production helicity amplitudes, $F^{(\mu)}_{\lambda_1\lambda_2}$, the spin density matrix elements are defined by

$$\rho_{\lambda_1\lambda_1'\lambda_2\lambda_2'} \equiv \frac{\sum_\mu F^{(\mu)}_{\lambda_1\lambda_2} F^{(\mu)*}_{\lambda_1'\lambda_2'}}{\sum_{\mu\lambda_1\lambda_2} |F^{(\mu)}_{\lambda_1\lambda_2}|^2}.$$

The normalisation is such that the trace of the matrix is unity. The initial state helicity sum runs over $\mu = \pm 1/2$ and the W particle helicities run over $\lambda_i, \lambda_i' = \pm 1, 0$.

The helicities of W particles can be determined from their centre-of-mass decay distribution asymmetries. The above definition of the $\rho_{\lambda_1\lambda_1'\lambda_2\lambda_2'}$ elements can be put [6] into the following form which is model independent and is directly applicable to experimental data corrected for backgrounds and detection efficiences:

$$\begin{aligned}
&\frac{d\sigma}{d(\cos\theta_{W^-})\,d(\cos\theta_1^*)\,d\phi_1^*\,d(\cos\theta_2^*)\,d\phi_2^*} \\
&= \frac{d\sigma}{d(\cos\theta_{W^-})}\left(\frac{3}{8\pi}\right)^2 \sum_{\lambda_1\lambda_1'\lambda_2\lambda_2'} \rho_{\lambda_1\lambda_1'\lambda_2\lambda_2'}(\cos\theta_{W^-}) \\
&\quad \times D_{\lambda_1\lambda_1'}(\theta_1^*, \phi_1^*) D_{\lambda_2\lambda_2'}(\theta_2^*, \phi_2^*). \qquad (1)
\end{aligned}$$

Here, θ_{W^-} is the angle of the W^- production with respect to the e^- beam, θ_1^* and θ_2^* are the polar decay angles of the W^- and W^+ in their rest frames and ϕ_1^*, ϕ_2^* are the corresponding azimuthal decay angles, as shown in Fig. 5.

[a] Deceased.

[b] e-mail: jan.timmermans@cern.ch

The functions $D_{\lambda\lambda'}$ are the theoretical decay distributions of the W particles in the helicity states specified by the λ indices. Precise definitions of the angles $\theta^*_{1,2}$ and $\phi^*_{1,2}$ and of the functions $D_{\lambda\lambda'}$ relevant to the present analysis are given in Sect. 3. It should be noted that the cross-section formula (1) is model independent regarding the WW production process.

The single-W particle spin density matrix $\rho_{\lambda\lambda'}$, derived from the WW spin density matrix $\rho_{\lambda_1\lambda'_1\lambda_2\lambda'_2}$ by summation over one of the indices $(1, 2)$, gives information about the polarisation of one W regardless of the state of the other. All nine elements of the single-W particle spin density matrix can be determined using the data from semi-leptonic events. This was done in [1] and [2, 3], where only the electron and muon decays of one W were used as the analyser of the W polarisation. The hadronic decays of W particles were not used because of the reasons outlined above and because the analysing power of polarisation in such decays is greatly reduced as the result of the severe practical difficulty to distinguish quark jets from anti-quark jets.

In the present study, it would ideally be desirable to measure the complete 9×9 matrix $\rho_{\lambda_1\lambda'_1\lambda_2\lambda'_2}$. As the result of the limitations in the polarisation information from the hadronic W decays, only a small part of the joint WW spin density matrix can be measured. It is possible to measure five (out of nine) diagonal elements ($\rho_{\lambda_1\lambda_1\lambda_2\lambda_2}$) plus nine complex off-diagonal elements. Instead of this incomplete set of individual matrix elements, the following three linear combinations of matrix elements are considered in this paper:

$$\begin{aligned} \rho_{LL} &= \rho_{0000}, \\ \rho_{TT} &= \rho_{++--} + \rho_{--++} + \rho_{----} + \rho_{++++}, \\ \rho_{LT} &= \rho_{++00} + \rho_{00++} + \rho_{--00} + \rho_{00--}. \end{aligned} \tag{2}$$

The quantities ρ_{LL}, ρ_{TT} and ρ_{LT} are composed of the diagonal elements of the full matrix and they can be interpreted as probabilities of the joint, i.e. correlated, polarisation states of the two Ws. The elements ρ_{TT} and ρ_{LT} do not distinguish between the + and – transverse helicities, and also the polarisations of the states $W^-_L W^+_T$ and $W^-_T W^+_L$ are combined. This is a reduced set of information about the WW polarisations but it is nevertheless very useful. The elements ρ_{TT}, ρ_{LT} and ρ_{LL} can be measured in semi-leptonic WW events because cancellations in the sums (2) imply that the incompleteness of the polarisation information in the hadronic W decays does not matter [6]. In Sect. 3 it will be shown how ρ_{TT}, ρ_{LT} and ρ_{LL} can be measured directly from the data without recourse to the individual spin density matrix elements in (2).

2 The experiment, treatment of data and simulation

2.1 The experiment

The DELPHI detector is described in detail in [7, 8] and its configuration during the LEP2 runs is given in [9]. The reference [9] gives a complete description of the selection of WW events in DELPHI. The present analysis uses the data taken at centre-of-mass energies between 189 and 209 GeV. The data are grouped into three sets at average energies of 189 GeV, 200 GeV and 206 GeV. The total integrated luminosity is 520 pb^{-1}, and the luminosity-weighted average energy of all data is 198.2 GeV. Jet reconstruction algorithms as well as electron and muon identification are also described in [9].

2.2 Selection of data and Monte Carlo simulation

2.2.1 Data selection

The initial selection procedure for the channels $\mu\nu q\bar{q}$ and $e\nu q\bar{q}$ is based on the typical topology of those events. As already mentioned, events from the $\tau\nu q\bar{q}$ channels are not included in this analysis and thus they are a part of the background. The starting values of the data cuts are those listed in [9]:

(i) visible event energy $\geq 40\%$ of the nominal centre-of-mass energy;
(ii) the event transverse energy ≥ 45 GeV;
(iii) the event must have at least one muon or one electron identified;
(iv) electron or muon candidate's momentum ≥ 20 GeV/c;
(v) charged lepton track angle with respect to the beam direction $\geq 20°$;
(vi) the total track multiplicity in each hadron jet ≥ 3;
(vii) reconstructed W^- and W^+ masses ≥ 50 GeV/c^2.[1]

The precise values of these cuts, in particular those on the event transverse energy and the minimum particle multiplicity in jets, were varied slightly for data taken at the three different average e^-e^+ energies. Three-constraint kinematic fits were then performed to the reaction $e^-e^+ \to W^-W^+$ on the selected data samples, requiring both Ws to have the same mass consistent with 80.4 GeV/c^2. Cuts on the χ^2 probability distribution were then applied, with the value of the cut (in the region 0.5%–1%) determined from the χ^2 distribution in each of the three data sets. The final sample, taken at all beam energies, consists of 800 electron plus 880 muon events. This sample is somewhat smaller than that reported in [9] because we require full functionality of all parts of DELPHI.

[1] The masses are calculated from the results of a preliminary 1-constraint kinematic fit to the reaction $e^-e^+ \to W^-W^+$.

Particle momenta and angles obtained from kinematic fitting have been used in the analysis of this experiment.

2.2.2 *Event simulation*

Simulation of events plays a crucial role in the experimental procedure to separate events corresponding to the reaction $e^-e^+ \to W^-W^+$, the "signal", from backgrounds. The signal is defined by the three CC03 Feynman diagrams shown in Fig. 1. These account only for a part of the four-fermion processes contributing to the data. In this experiment a customised version [10] of the WPHACT [11, 12] generator program was used to simulate all the four-fermion processes. The DELPHI WPHACT program includes reweighting for the Double Pole Approximation (DPA) radiative corrections and the possibility to compute the matrix elements of different subsets of Feynman diagrams. The weights are the ratios of the squared matrix element for WW production only via the CC03 diagrams to that for production via the full set of four-fermion processes. It is thus possible to simulate CC03 events corresponding to production via the CC03 diagrams with or without inclusion of other four-fermion processes.

In addition to the four-fermion background, there is a significant two-fermion background, mostly from $\bar{q}q\gamma$ final states. This background has been simulated using the KK2F generator [13].

The generators were interfaced to the PYTHIA [14, 15] hadronisation program. Large simulated samples, of the order of 10^6 events, were produced by the programs listed above, interfaced to the DELPHI detector simulation program DELSIM [7, 8].

2.3 Reconstruction of events

Event reconstruction efficiencies were determined using events simulated with the WPHACT Monte Carlo program adapted for DELPHI [10]. The efficiency is defined as the ratio of the number of reconstructed CC03 WPHACT Monte Carlo events to the number of generated events, including all four-fermion channels.

Efficiencies are determined as functions of $\cos\theta_{W^-}$, $\cos\theta_1^*$ and $\cos\theta_2^*$, defined in Sect. 1. The resulting reconstruction efficiency table is a $5 \times 5 \times 7$ matrix corresponding to 7 bins of $\cos\theta_{W^-}$, as defined in Sect. 4.2, and 5 equal size bins for each of $\cos\theta_1^*$ and $\cos\theta_2^*$. The reconstruction efficiency matrices were determined separately for the electron and muon event samples at the three centre-of-mass energies. Typical values of the reconstruction efficiency, ϵ, as a function of $\cos\theta_{W^-}$ are 0.65 to 0.74 when integrated over all $\cos\theta_1^*$ and $\cos\theta_2^*$. The values of ϵ as a function of $\cos\theta_1^*$ (or of $\cos\theta_2^*$), averaged over $\cos\theta_{W^-}$, vary over the range 0.6 to 0.8.

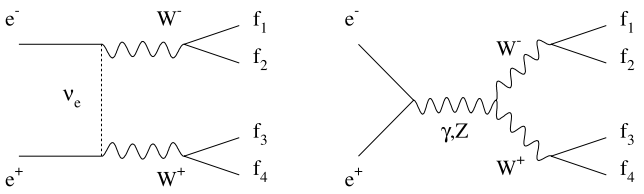

Fig. 1 CC03 diagrams, i.e. the lowest order contributions to the amplitude for W^-W^+ production. ($f_{1,2,3,4}$ stand for the appropriate fermions.)

2.4 Treatment of backgrounds

The dominant backgrounds to the selection of $e\nu jj$ and $\mu\nu jj$ events (where j implies a hadronic jet) can be divided into two groups.

(a) *Events which result from problems in reconstruction or selection procedures.* The dominant contribution to this class of events comes from two-fermion final states, in particular from $\bar{q}q\gamma$. Other contributions come from neutral current four-fermion final states which might be misidentified as $e\nu jj$ or, more rarely, as $\mu\nu jj$. Misidentified charged current events $\tau\nu jj$ are also potentially a background in this experiment.

(b) *The non-CC03 charged current four-fermion contributions to the global $\mu\nu jj$ or $e\nu jj$ final states.* In contrast to the background (a), this background would exist even in a perfect detector and an ideal experimental event selection procedure. A number of the charged current four-fermion diagrams in this category can interfere with the CC03 amplitude.[2]

Following the treatment in [9], the backgrounds requiring special attention are:

(i) the τ events, $WW \to \tau\nu jj$ (belonging to group (a));
(ii) various four-fermion processes which for experimental or other reasons lead to the same final state as the reaction $e^-e^+ \to W^-W^+$ (such backgrounds may arise from groups (a) and (b));
(iii) two-fermion events, mostly $\bar{q}q\gamma$ interactions (group (a)).

Discussion of each of these background sources follows in turn.

- The background from source (i) has been investigated by passing the simulated $\tau\nu jj$ events through the normal analysis chain and requiring $e\nu q\bar{q}$ or $\mu\nu q\bar{q}$ fits. The background from this source turns out to be negligible as the result of kinematic cuts and fitting.

[2] As a consequence of the finite W width, any Monte Carlo generator of $e^-e^+ \to W^-W^+$ events at low energy must be a four-fermion generator in order to satisfy gauge invariance.

- The background (ii) is due both to charged current and neutral current events.

The charged current processes consist of the three CC03 diagrams plus seven diagrams with s-channel exchange of Z^0/γ, leading to the production of only one W. There are also ten charged current diagrams corresponding to t-channel processes which give rise to one W. The latter diagrams can give rise to backgrounds only in the electron final state $e\nu jj$.

The neutral current four-fermion states have two quarks and two leptons of the same flavour. If one of the electrons is not identified in the detector, the event may be classified as belonging to the channel $WW \to e\nu jj$ and may satisfy the criteria for an acceptable kinematic fit. Altogether, the four-fermion backgrounds affect the electron channel, $e\nu q\bar{q}$, more than the muon channel $\mu\nu q\bar{q}$.

It was found that the non-CC03 four-fermion background in the real events could be efficiently reduced to a level less than 4% by tuning the kinematic cuts and the χ^2 cuts, as described in Sect. 2.2. The effectiveness of the removal of this class of background events can be demonstrated in the following way: Starting from a large sample of generated events, two data samples were produced making use of the event reweighting facilities in WPHACT. Sample A contained predominantly the CC03 events and sample B the non-CC03 four-fermion background. Each sample was processed through the experimental procedure described in Sect. 2.2. The event ratio $\Pi = \mathrm{B/A}$ represents the proportion of the four-fermion background in the WW signal to be expected in the final sample of the real data. This quantity is of the order of 3% and is weakly dependent on $\cos\theta_{W^-}$. A plot of Π for WPHACT data at 200 GeV is shown in Fig. 2(a). The results for other run energies are similar.

A further test of the effectiveness of the method for dealing with the non-CC03 four-fermion background is to apply the analysis to a simulated data set where the expected result is known. For this purpose, the element ρ_{00} of the single-W spin density matrix $\rho_{\lambda\lambda'}$ is evaluated. This test was carried out for data generated at all three run energies, but here only the results from WPHACT at 200 GeV are shown. In Fig. 2(b), triangle symbols are used to plot the value of ρ_{00} obtained from the WPHACT generated events using all the four-fermion diagrams, with no cuts except for the final kinematic χ^2 selection. Star symbols are used to plot the value of ρ_{00} after the same generated events have been passed through the complete selection procedure described in Sect. 2.2. The smooth solid curve is from an analytic calculation using only the CC03 diagrams. The conclusion drawn from this is that the procedure adopted for analysing the data removes essentially all the four-fermion background, leaving events which are attributable to the CC03 signal.[3]

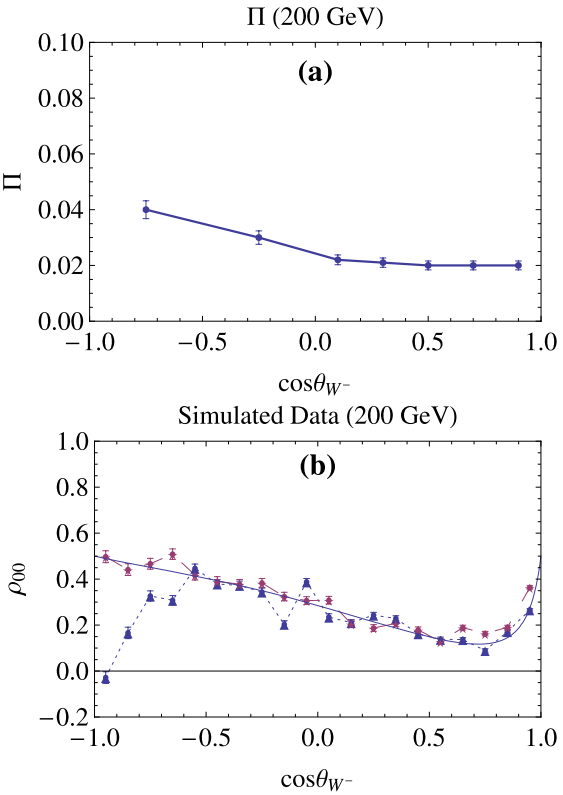

Fig. 2 (**a**) Plot of the quantity Π, defined in the text, as a function of $\cos\theta_{W^-}$ for data simulated at 200 GeV. (**b**) Plots of the density matrix element ρ_{00} evaluated from four-fermion events generated at 200 GeV with WPHACT before (*triangle symbols*) and after (*star symbols*) the event reconstruction procedure, including application of data cuts and kinematic fitting. The *smooth curve* is from an analytic calculation using CC03 diagrams

The residue of the non-WW four-fermion background in the real data at all run energies is estimated to be at the level of $3 \pm 2\%$, the uncertainty is due to combining results from different energies.

- The background process (iii) is potentially very serious because the cross-section for $\bar{q}q\gamma$ production is about an order of magnitude larger than that for the WW signal. Although the topology of the $\bar{q}q\gamma$ events is quite different from that of the WW events, the reconstructed events of the background can resemble and fit the WW reaction. The problem of how to suppress this background has been investigated using the KK2F Monte Carlo generator [13].

[3] The plot made with triangle symbols in Fig. 2(b) shows a strong dip near $\cos\theta_{W^-} = -1$ and some fluctuations up to about $\cos\theta_{W^-} = 0$. These effects are caused by some of the four-fermion backgrounds in the simulated raw data. In particular, the background events whose W particles are not genuine spin 1 states tend to interfere destructively with the true Ws in the ρ_{00} evaluation.

It is found that this background shows a very characteristic kinematic signature in the distribution of the quantities $\cos\Theta_{ll}$ and $\cos\Theta_{jj}$, where Θ_{ll} is the angle between the momentum vectors of the two leptons (one charged and a neutrino) coming from one W and Θ_{jj} is the angle between the jets from the accompanying W, with quantities defined in the laboratory frame (i.e. the reaction centre-of-mass).[4] The presence of the $\bar{q}q\gamma$ background shows up as accumulations of events at $\cos\Theta_{ll} \sim -1$ and $\cos\Theta_{jj} \sim -1$.

After the usual cuts and kinematic fitting, the real data samples show peaks in the $\cos\Theta_{ll}$ and $\cos\Theta_{jj}$ distributions indicating small but non-negligible contamination from the $\bar{q}q\gamma$ background. Below it will be shown that the contamination is of the order of 10% at 189 GeV. This contamination has to be evaluated accurately because it affects the angular distribution of W decays. The kinematics of the W decay in the laboratory frame of the reaction is such that the distributions of the quantities $\cos\Theta_{ll}$ and $\cos\Theta_{jj}$ have large discriminating power against the $\bar{q}q\gamma$ background. This enables the magnitude of the background to be determined and also provides a means of reducing the background by applying cuts on these distributions or by applying suitable event weights. Only the method of weights has been used in dealing with this background.

Figures 3(a) and 3(b) show, respectively, simulations of the $\cos\Theta_{ll}$ and $\cos\Theta_{jj}$ distributions at 189 GeV. The curves labelled WW were obtained from the WPHACT simulation of CC03, while the curves labelled $\bar{q}q\gamma$ are from the KK2F simulation of this background. At this stage of the analysis, the relative magnitudes of the WW and $\bar{q}q\gamma$ components are still unknown; therefore, the two curves are normalised to the same number of events. Figures 4(a) and 4(b) show the results of a least squares fit to the relative contributions from WW and $\bar{q}q\gamma$, using the distributions from the simulated events, to the real data distributions. The fit to the 189 GeV data requires contributions of 90% from WW and $10 \pm 2\%$ from $\bar{q}q\gamma$, while the same analysis applied to the data at 200 GeV and 206 GeV require a $5 \pm 2\%$ $\bar{q}q\gamma$ background contribution at both energies.

This determination of the relative magnitude of the $\bar{q}q\gamma$ background with respect to the WW signal enables a combined WPHACT plus KK2F simulation of the real data. The combined simulation was subsequently used to derive weighting factors, p, defining the purity of the WW signal in each bin of $\cos\theta_{W^-}$, $\cos\theta_1^*$ and $\cos\theta_2^*$, using the same binning as that used for the reconstruction efficiencies, ϵ. The application of the weight factors p is described in the following section.

[4]The momentum vectors are taken from the constrained kinematic fit.

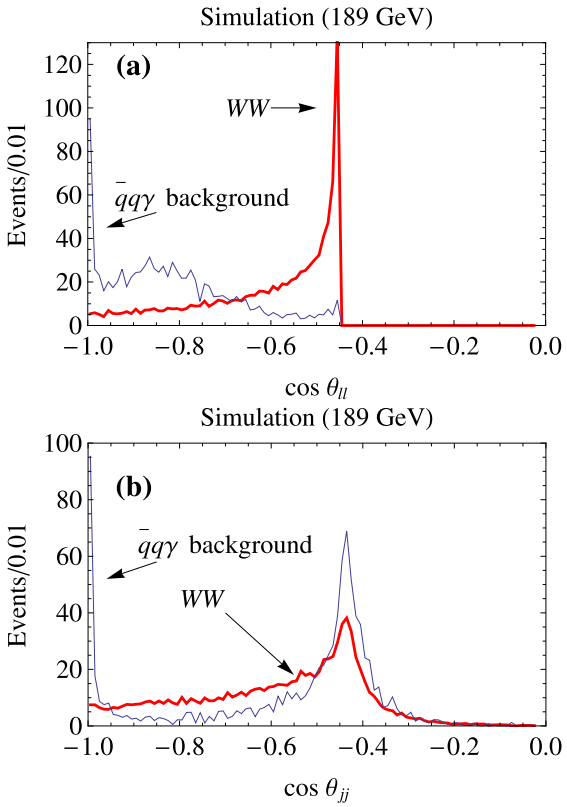

Fig. 3 Distributions (**a**) of $\cos\Theta_{ll}$ and (**b**) of $\cos\Theta_{jj}$ in the $\bar{q}q\gamma$ background and in the reaction $e^-e^+ \to W^-W^+$ from data simulated at 189 GeV. (The angles Θ_{ll} and Θ_{jj} are defined in the text.) The curves labelled $\bar{q}q\gamma$ and WW are normalised to the same number of events

3 Analysis

W decays are well described by the V–A theory of the charged current weak interactions. The theory gives the functions $D_{\lambda\lambda'}(\theta^*, \phi^*)$ required for evaluating the spin density matrix elements $\rho_{\lambda_1\lambda_1'\lambda_2\lambda_2'}$ by applying (1) to the data. The W^- production angle, θ_{W^-}, and the $W^{-,+}$ decay angles $\theta_{1,2}^*$, $\phi_{1,2}^*$, which specify the direction of the final state fermion in the rest frame of the W^- and of the final state anti-fermion in the rest frame of the W^+, are defined in Fig. 5.

As already pointed out, fermions can be distinguished from anti-fermions in the W leptonic decays but not so in the hadronic decays. However, some of the decay functions $D_{\lambda\lambda'}(\theta^*, \phi^*)$ are invariant under the transformation which rotates the momentum vector of a fermion in the W rest frame into the direction of its opposite anti-fermion vector. These functions will be called symmetric and designated by $D^{(s)}$. Consequently, the symmetric D functions and the symmetric parts of the non-symmetric D functions can be used to analyse the polarisation of the Ws decaying into the purely hadronic final states. The polarisation information obtained is thus incomplete but, nevertheless, it is useful and, in particular, the quantities ρ_{TT}, ρ_{LT} and ρ_{LL} can

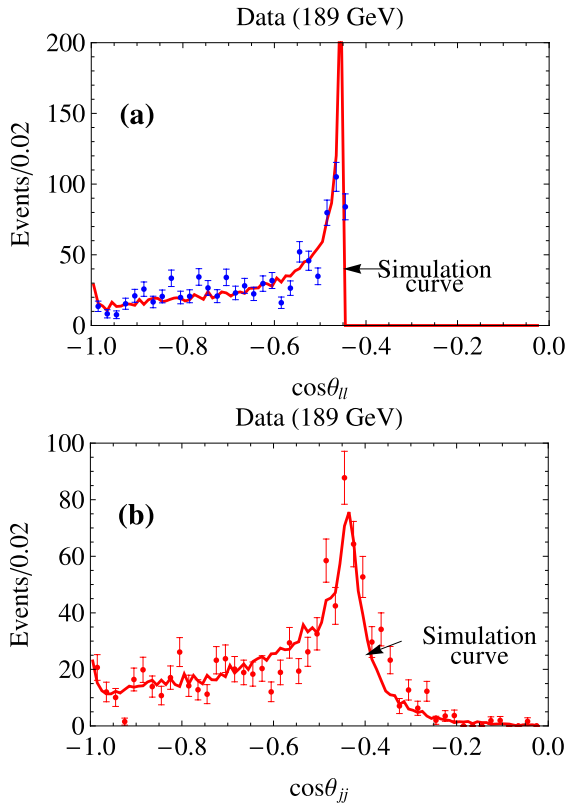

Fig. 4 Distributions (**a**) of $\cos\Theta_{ll}$ and (**b**) of $\cos\Theta_{jj}$ for the real data at 189 GeV. The superimposed curves are the result of a fit using simulated samples of $\bar{q}q\gamma$ and WW events

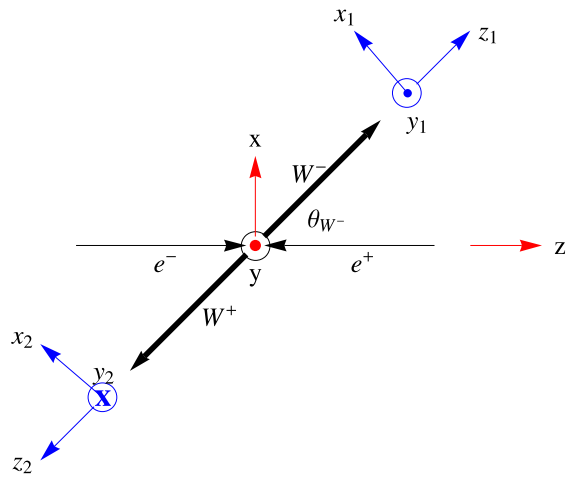

Fig. 5 Diagram of the momentum vectors in the reaction plane of the process $e^-e^+\to W^-W^+$. The two right-handed sets of orthogonal axes (x_1,y_1,z_1) and (x_2,y_2,z_2) in the respective rest frames of the W^- and W^+ are also shown. The polar angles θ_1^* and θ_2^* of the momentum vectors of the two-body decays of the W^- and W^+ are measured with respect to the axes z_1 and z_2

be obtained from the data using only the symmetric decay distributions in both associated Ws.

The theoretical formalism for extracting ρ_{TT}, ρ_{LT} and ρ_{LL} from the data is based on (1) with two modifications.

(i) Equation (1) is integrated over the full range of ϕ_1^* and ϕ_2^*. This removes the functions $D_{\lambda\lambda'}$ having $\lambda'\neq\lambda$ and eliminates all non-diagonal elements of the matrix $\rho_{\lambda_1\lambda_1'\lambda_2\lambda_2'}$. The following three decay functions remain:

$$\begin{aligned} D_{++}(\theta^*) &= \frac{1}{2}(1-\cos\theta^*)^2,\\ D_{00}(\theta^*) &= \sin^2\theta^*,\\ D_{--}(\theta^*) &= \frac{1}{2}(1+\cos\theta^*)^2. \end{aligned} \tag{3}$$

(ii) Furthermore, only the symmetric parts, $D^{(s)}_{\lambda\lambda}$, of the functions in (3) are to be used:

$$\begin{aligned} D^{(s)}_{++}(\theta^*) &= D^{(s)}_{--}(\theta^*) = \frac{1}{2}\left(1+\cos^2\theta^*\right),\\ D^{(s)}_{00}(\theta^*) &= \sin^2\theta^*. \end{aligned}$$

Pursuing the above steps, the following modified form [6] of (1) is obtained:

$$\begin{aligned} &\frac{d\sigma^{(s,s)}}{d(\cos\theta_{W^-})\,d(\cos\theta_1^*)\,d(\cos\theta_2^*)}\\ &= \left(\frac{3}{4}\right)^2\left(\frac{d\sigma}{d(\cos\theta_{W^-})}\right)\\ &\quad\times\left\{\rho_{TT}(\cos\theta_{W^-})D^{(s)}_{++}\left(\theta_1^*\right)D^{(s)}_{++}\left(\theta_2^*\right)\right.\\ &\quad+\rho_{LT}(\cos\theta_{W^-})\left[D^{(s)}_{00}\left(\theta_1^*\right)D^{(s)}_{++}\left(\theta_2^*\right)\right.\\ &\quad\left.+D^{(s)}_{++}\left(\theta_1^*\right)D^{(s)}_{00}\left(\theta_2^*\right)\right]\\ &\quad\left.+\rho_{LL}(\cos\theta_{W^-})D^{(s)}_{00}\left(\theta_1^*\right)D^{(s)}_{00}\left(\theta_2^*\right)\right\}, \end{aligned} \tag{4}$$

where ρ_{TT}, ρ_{LL} and ρ_{LT} have been defined in (2). The above equation assumes CP invariance, i.e. that the joint polarisations $W_L^-W_T^+$ and $W_T^-W_L^+$ are equal. The superscript (s,s) indicates that only the symmetric decays of both Ws are considered.

The angular distribution of the W^- production is not used explicitly in the data analysis for measuring the correlations ρ_{TT}, ρ_{LT} and ρ_{LL}. However, it is appropriate to examine the shape of the distribution $dN/d(\cos\theta_{W^-})$ as a test of the quality of the data. Figure 6 shows the angular distribution of the W^- in the present data at all energies combined, compared to the WPHACT prediction. The agreement with WPHACT is satisfactory. The distribution shown also agrees well with that in the DELPHI publication on the WW production cross-section [9].

Before using the functions (3) to determine the intensities of different helicity states in the data, these functions must be transformed to a related set of functions with the property

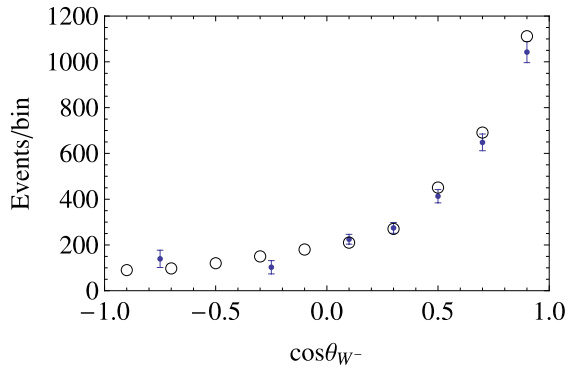

Fig. 6 Angular distribution of W^- production. *Points with error bars* are the experimental data; the errors shown are statistical only. The data binning is explained in Sect. 4.2. The *small circles* show the predictions of the WPHACT simulation

that each one is non-orthogonal to only one in the group of distribution functions (3) and is orthogonal to the other two. These functions are called projectors [16] and they can easily be worked out from (3). The projector functions needed to extract ρ_{TT}, ρ_{LT} and ρ_{LL} are

$$\begin{aligned} \Lambda_L &= 2 - 5\cos^2\theta^*, \\ \Lambda_T &= 5\cos^2\theta^* - 1. \end{aligned} \tag{5}$$

These projectors are normalised to give the spin density matrices in the standard representation [6, 16]. The quantities ρ_{LL}, ρ_{TT} and ρ_{LT} are obtained from the data by evaluating the following sums:

$$\begin{aligned} \rho_{LL} &= \frac{1}{N_w}\sum_i \Lambda_L\left(\theta^*_{1i}\right) w_i \Lambda_L\left(\theta^*_{2i}\right), \\ \rho_{TT} &= \frac{1}{N_w}\sum_i \Lambda_T\left(\theta^*_{1i}\right) w_i \Lambda_T\left(\theta^*_{2i}\right), \\ \rho_{LT} &= \frac{1}{N_w}\Bigg(\sum_i \Lambda_L\left(\theta^*_{1i}\right) w_i \Lambda_T\left(\theta^*_{2i}\right) \\ &\quad + \sum_i \Lambda_T\left(\theta^*_{1i}\right) w_i \Lambda_L\left(\theta^*_{2i}\right)\Bigg), \end{aligned} \tag{6}$$

where summations are over all events i. $N_w = \sum_i w_i$ is the sum of all event weights w_i, and the event weights w are defined as

$$w = \frac{p}{\epsilon},$$

where p is the WW purity factor, defined as in Sect. 2.4, for each bin of $(\cos\theta_{W^-}, \cos\theta^*_1, \cos\theta^*_2)$, and ϵ is the event reconstruction efficiency in that bin, defined in Sect. 2.3. In these formulae, index 1 refers to W^- and index 2 refers to W^+.

Monte Carlo studies have shown that the correlations ρ_{LT}, ρ_{LL}, ρ_{TT} extracted from small samples of data (such as we have at each of the three energy points considered) are subject to large statistical fluctuations. These fluctuations are much larger than those encountered in the determination of the single-W spin density matrix elements. Because of that, all 1680 semi-leptonic electron and muon events have been taken as one sample for measuring ρ_{LT}, ρ_{LL} and ρ_{TT}. The sum of weights of these events is 2844.

The fact that events which we analyse here as one sample come from a spread of centre-of-mass energies presents no difficulty because the theoretical predictions which we want to test can be modified to take into account the spread. In particular, the Standard Model [6] predicts a negligible variation of ρ_{TT}, ρ_{LT} and ρ_{LL} over the energy range of this experiment.

4 Results

4.1 Systematic effects and errors

4.1.1 Data cuts

Systematic effects resulting from residual backgrounds in real events have been estimated by processing the data several times with small variations in the cuts and, separately, with various χ^2 cuts. Variations in the resulting values of the spin density matrix elements ρ_{LT}, ρ_{LL}, ρ_{TT} amount to 10% of their statistical error. This is interpreted as the magnitude of the systematic uncertainty and it is neglected.

4.1.2 Hadron jet reconstruction

Problems in hadron jet reconstruction [9] can give rise to a shift in $\cos\theta_{W^-}$ with the further consequence that the reconstruction efficiency is read from the wrong cell of the ϵ matrix. This migration and its effects have been examined using simulated events. The resulting uncertainty on θ_{W^-} is small: it varies from $\pm 2°$ at large angles to $\pm 5°$ at small angles, i.e. in the forward direction[5]. This is negligible by comparison with the sizes of the $\cos\theta_{W^-}$ bins. The effect of this migration on the spin density matrix elements has been examined by moving the simulated events randomly by the above uncertainty in $\cos\theta_{W^-}$. The effect of this variation on the joint spin density matrix elements is 5%–8% of the statistical uncertainty and is therefore considered to be negligible.

Also, jet reconstruction problems can produce wrong momentum vectors of the W hadronic decay products. This has been investigated by processing the same events using different jet algorithms as described in reference [9]. No statistically significant effect was found when comparing the spin density matrix elements distributions obtained in these tests.

[5]This uncertainty includes a problem in the simulation of charged particle tracks in the forward region of DELPHI. This problem and its solution are discussed in two recent DELPHI papers [17, 18].

4.1.3 Lepton charge determination

Tracks at small angle with respect to the e^- and e^+ beams are susceptible to wrong charge determination. This problem is essentially eliminated [1] by the 20° cut on the lepton polar angle (see Sect. 2.2). The effect of this cut on the spin density matrix elements has been examined by simulation of events and was found to be negligible.

4.1.4 Radiative corrections

The effect of the initial state radiation is essentially removed by the appropriate energy cut. The final state radiative corrections are implemented through the Double Pole Approximation in the WPHACT reweighting. The uncertainty due to the radiative corrections on the spin density matrix elements is negligible. This has been established by a comparison of the spin density matrix elements evaluated from events generated with WPHACT, including the corrections, with the same elements calculated analytically [6, 16] without the radiative corrections. This can be understood because the spin density matrix elements are ratios of quantities which are similarly affected by the radiative effects.

4.1.5 Use of a fixed W mass in kinematic fitting of events

Three-constraint kinematic fits of the reaction events are needed in order to separate the signal from a large background. Fixing the masses of both Ws in the reaction to the same value, as stated in Sect. 2.2.1, does not cause noticeable distortions of angular distributions and other quantities needed for the physics analysis. This has been checked by comparing the results obtained from the three-constraint fits with those from the one-constraint fits of the same events. As a further test, somewhat different fixed values of the W mass were tried. Statistically insignificant differences in the results were found.

4.2 Presentation of results

The measured values of ρ_{TT}, ρ_{LT} and ρ_{LL} as functions of $\cos\theta_{W^-}$ are shown in Fig. 7. Because the number of events in the negative hemisphere of W^- production is much smaller than that in the positive hemisphere, the data have been divided into two bins in the negative hemisphere and five bins in the positive hemisphere. (The positive hemisphere is in the direction of the e^- beam.) It is easy to derive from formulas (5) and (6) that the condition

$$\rho_{LL} + \rho_{TT} + \rho_{LT} = 1 \tag{7}$$

is valid on an event by event basis and is hence automatically satisfied by all data samples.

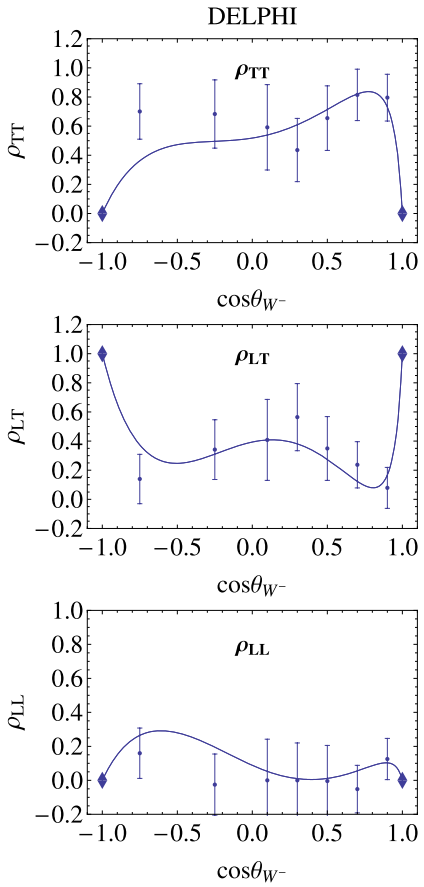

Fig. 7 Variation of the spin density matrix elements TT, LT and LL with the cosine of the W^- production angle, θ_{W^-}, at the average energy of 198.2 GeV. *Points with error bars* are the measured data, and the *curves* are the Standard Model CC03 predictions. The *diamond symbols* indicate the points predicted by angular momentum conservation, as explained in the text in Sect. 4.2

The curves shown in the plots are the Standard Model calculations based on the CC03 diagrams evaluated at 198.2 GeV using the expressions in [16]. The error bars shown in the plots are statistical, the systematic errors being negligible by comparison. Errors on all measured quantities are evaluated from the data as standard deviations. The distributions of the errors are approximately Gaussian.

Some events can contribute negative numbers to the sums shown in (6) while the final result is positive. However, if a particular correlation quantity ρ is very small, the measurement errors, which have a Gaussian distribution, can lead to an overall result which is negative. This happens in three out of the seven measured values of ρ_{LL} presented here. They are very small negative quantities, consistent with zero within the measurement errors, i.e. $|\rho_{LL}| < \delta\rho_{LL}$, where $\delta\rho_{LL}$ is the measurement error. These negative values of ρ_{LL} are included in Fig. 7. The condition (7) still holds in these cases as a result of the properties of the projector functions (5). Of course, the physical quantities ρ should satisfy the condition $\rho \geq 0$. Several methods of adjusting the results

to satisfy the positivity condition were tried, but not used in the end because they introduce biases that are more harmful than the small negative numbers among the results.

The data bins in Fig. 7 are too wide to show the possibly rapid variations of the measured quantities very near to $\cos\theta_{W^-} = \pm 1$. However, the exact values of these correlations at $\cos\theta_{W\_} = \pm 1$ follow from the conservation of angular momentum. Neglecting the electron mass, the vector and axial-vector interactions involved at the e^- and e^+ vertices cause the initial e^- and e^+ to interact only when their helicities are opposite. Thus, the initial system has total helicity ± 1 and when the final state is collinear with the e^-e^+ beams its total helicity must be the same. This means that at $\theta_{W^-} = 0$ or π, ρ_{LT} must be 1 and, at the same time, $\rho_{LL} = \rho_{TT} = 0$. These values have been indicated with diamond-shaped symbols in Fig. 7.

Because of the low statistics in this experiment, it is useful to examine the values of ρ_{TT}, ρ_{LT} and ρ_{LL} averaged over all bins of $\cos\theta_{W^-}$ and to compare them with the predictions of the Standard Model. The results are shown in Table 1.

The differential polarisation cross-sections $d\sigma_{TT}/d(\cos\theta_{W^-})$, $d\sigma_{LT}/d(\cos\theta_{W^-})$ and $d\sigma_{LL}/d(\cos\theta_{W^-})$ are related to ρ_{TT}, ρ_{LT}, ρ_{LL} through the equation

$$\frac{d\sigma_{TT}(\cos\theta_{W^-})}{d(\cos\theta_{W^-})} = \frac{d\sigma(\cos\theta_{W^-})}{d(\cos\theta_{W^-})}\rho_{TT}(\cos\theta_{W^-}), \tag{8}$$

plus the analogous expressions for the states LT and LL. The first term on the right-hand side of (8) can be replaced by the data points from the angular distribution shown in Fig. 6, normalised to the total cross-section for $e^-e^+ \to W^-W^+$ at the average energy of the experiment. The relevant measured cross-section is $\sigma = (17.07 \pm 0.57)$ pb at 198.2 GeV. It has been obtained by an interpolation of the DELPHI measurements [9] which cover the range 161 to 209 GeV. With this result and the measured ρ_{TT}, ρ_{LT}, ρ_{LL} as functions of $\cos\theta_{W^-}$, one obtains the differential polarisation cross-sections shown in Fig. 8. Integration over $\cos\theta_{W^-}$ yields the total polarisation cross-sections σ_{TT}, σ_{LT} and σ_{LL} shown in Table 2.

These results are in good agreement with the Standard Model predictions. The polarisation fractions expressed in terms of the density matrix elements (Table 1) and those expressed in terms of the cross-section ratios (Table 2) are different expressions of the two-particle polarisation correlations in the reaction. Measurement errors of the polarisations are themselves strongly correlated. The extent of all the correlations will be shown in Fig. 9(b).

Table 1 Measured values of ρ_{TT}, ρ_{LT} and ρ_{LL}, averaged over $\cos\theta_{W^-}$, compared with the predictions of the Standard Model. Errors are statistical

$\bar{\rho}$	Measured fraction	Standard Model
$\bar{\rho}_{TT}$	$67 \pm 8\%$	63.0%
$\bar{\rho}_{LT}$	$30 \pm 8\%$	28.9%
$\bar{\rho}_{LL}$	$3 \pm 7\%$	8.1%

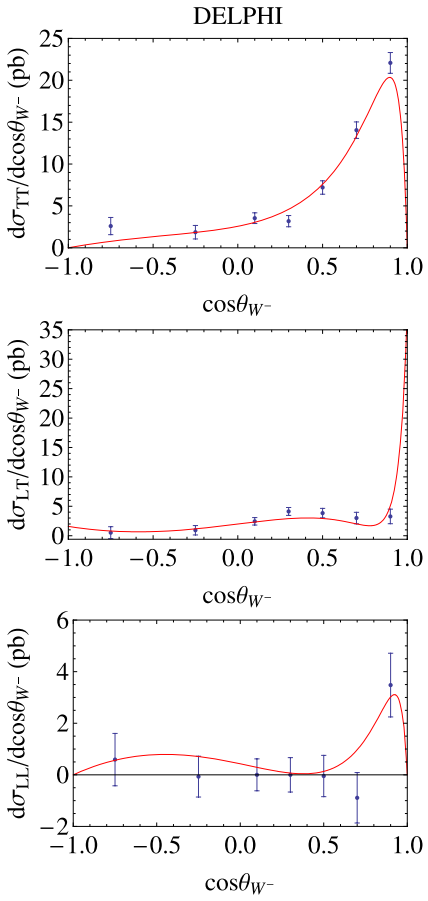

Fig. 8 Variation of the differential cross-sections TT, LT and LL as functions of the cosine of the W^- production angle, θ_{W^-}. *Points with error bars* are the measured data; the *curves* are the Standard Model CC03 predictions for the average energy of 198.2 GeV

Table 2 Measured values of the total cross-sections σ_{TT}, σ_{LT} and σ_{LL}, at the average energy of 198.2 GeV, compared with the predictions of the Standard Model. Also: Measured values of the ratios σ_{TT}/σ, σ_{LT}/σ and σ_{LL}/σ, at the average energy of 198.2 GeV, compared with the predictions of the Standard Model

σ	Measured cross-section	Standard Model
σ_{TT}	(12 ± 1) pb	(10.57 ± 0.05) pb
σ_{LT}	(4 ± 1) pb	(4.95 ± 0.02) pb
σ_{LL}	(1 ± 1) pb	(1.40 ± 0.01) pb
σ Ratios	Measured ratio	Standard Model
σ_{TT}/σ	0.70 ± 0.06	0.625 ± 0.003
σ_{LT}/σ	0.23 ± 0.06	0.292 ± 0.001
σ_{LL}/σ	0.06 ± 0.06	0.083 ± 0.001

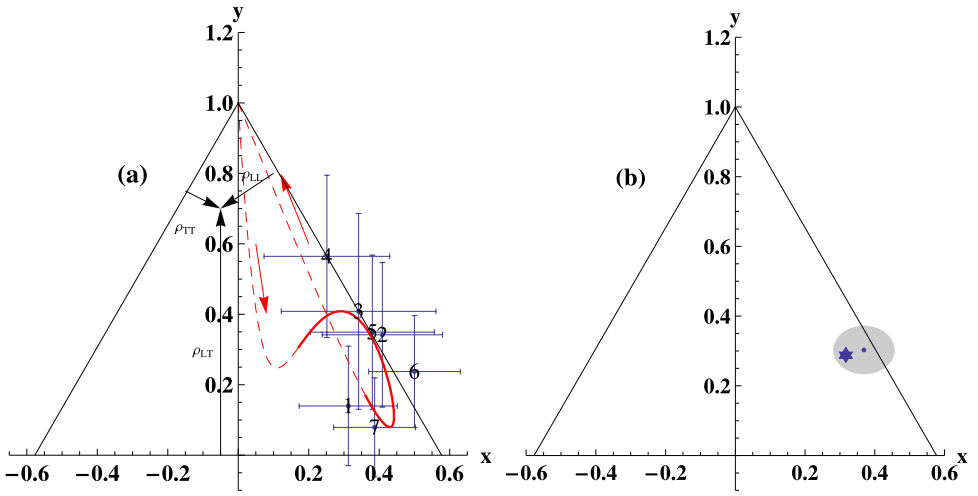

Fig. 9 (**a**) is the joint plot of the TT, LT and LL correlation data shown in Fig. 7. The coordinates x and y are defined in the text. The points are numbered 1–7, the first one corresponding to the data bin in $\cos\theta_{W^-}$ at -0.75 and the last one to the bin at $\cos\theta_{W^-} = +0.9$. The *curve* inside the triangle plot is explained in the text. (**b**) shows the (x, y) point obtained as the average of the points in (**a**). The shaded area is one standard deviation around the average (x, y) point. The *star symbol* shows the corresponding point predicted by the Standard Model

5 Discussion and conclusions

The measurements of the total cross-section for the reaction $e^-e^+ \to W^-W^+$ by ALEPH, DELPHI, L3 and OPAL [19], have successfully tested the predicted gauge coupling cancellations in this reaction. The direct measurement of the longitudinal cross-section for the *single* (i.e. uncorrelated) W production [1–3] is an important test of the same cancellation because the cause of the potential divergence of the cross-section is in the longitudinal parts. The measurement of the *joint* WW helicity states presented in this paper is an advance towards a more complete test of the Standard Model in the context of the WW reaction. Our measurement of $\sigma(e^-e^+ \to W_L W_L)$ is consistent both with zero and with the small value predicted by the Standard Model. This confirms that the probability of longitudinal W production is predominantly in association with a transverse W.

Figure 7 shows good agreement between the data and the Standard Model over the range of $\cos\theta_{W^-}$ where there are sufficient data. An important aspect of these results is the interrelation between the three spin density correlations ρ_{TT}, ρ_{LL} and ρ_{LT} determined in this analysis. These quantities can be displayed in one common plot due to the fact that they satisfy the condition (7). Thus, they can be plotted in a triangle plot, as shown in Fig. 9. Data can be plotted directly as indicated with arrows on the left side of Fig. 9(a) or by using Cartesian coordinates x and y,

$$x = \frac{1}{\sqrt{3}}(\rho_{TT} - \rho_{LL}), \qquad y = \rho_{LT}.$$

In Fig. 9(a) there are seven data points, each one corresponding to a different bin of $\cos\theta_{W^-}$. Error bars are also shown. The curve inside the triangle is the locus of points (x, y) calculated using CC03 diagrams. Each point on the curve corresponds to one particular value of $\cos\theta_{W^-}$. The point corresponding to $\cos\theta_{W^-} = -1$ is at the top vertex of the triangle. Further points are distributed as indicated by the arrows along the curved line and the last point (for $\cos\theta_{W^-} = +1$) is back at the top vertex. The solid part of the curve indicates the region where most of our data are located.

Figure 9(b) shows the average values, $\bar{\rho}_{TT}$, $\bar{\rho}_{LT}$ and $\bar{\rho}_{LL}$, of the spin density matrix elements of Table 1, presented in a triangle plot. The shaded area is the one standard deviation region around the average point (x, y). The star symbol is at the point predicted by the Standard Model using the CC03 diagrams.

It is clear that the TT correlation probability is large, the LT correlations are next in strength and the LL correlations are small. These are some of the most important features of the Standard Model predictions for the reaction $e^-e^+ \to W^-W^+$.

In spite of the limitations due to low statistics, these results show that the salient features of the Standard Model predictions for the W–W polarisation correlations are compatible with our data. This provides an additional test of the gauge theory relations between the $\mathrm{SU}(2)_L \otimes \mathrm{SU}(1)_Y$ couplings.

Acknowledgements We are greatly indebted to our technical collaborators, to the members of the CERN-SL Division for the excellent performance of the LEP collider, and to the funding agencies for their support in building and operating the DELPHI detector.

We acknowledge in particular the support of Austrian Federal Ministry of Education, Science and Culture, GZ 616.364/2-III/2a/98, FNRS–FWO, Flanders Institute to encourage scientific and technological research in the industry (IWT) and Belgian Federal Office for Scientific, Technical and Cultural affairs (OSTC), Belgium, FINEP, CNPq, CAPES, FUJB and FAPERJ, Brazil, Ministry of Education of the Czech Republic, project LC527, Academy of Sciences of the Czech Republic, project AV0Z10100502, Commission of the European Communities (DG XII), Direction des Sciences de la Matière, CEA, France, Bundesministerium für Bildung, Wissenschaft, Forschung und Technologie, Germany, General Secretariat for Research and Technology, Greece, National Science Foundation (NWO) and Foundation for Research on Matter (FOM), The Netherlands, Norwegian Research Council, State Committee for Scientific Research, Poland, SPUB-M/CERN/PO3/DZ296/2000, SPUB-M/CERN/PO3/DZ297/2000, 2P03B 104 19 and 2P03B 69 23 (2002–

2004), FCT—Fundação para a Ciência e Tecnologia, Portugal, Vedecka grantova agentura MS SR, Slovakia, Nr. 95/5195/134, Ministry of Science and Technology of the Republic of Slovenia, CICYT, Spain, AEN99-0950 and AEN99-0761, The Swedish Research Council, The Science and Technology Facilities Council, UK, Department of Energy, USA, DE-FG02-01ER41155, EEC RTN contract HPRN-CT-00292-2002.

References

1. J. Abdallah et al. (DELPHI Collaboration), Eur. Phys. J. C **54**, 345 (2008)
2. G. Abbiendi et al. (OPAL Collaboration), Phys. Lett. B **585**, 223 (2004)
3. P. Achard et al. (L3 Collaboration), Phys. Lett. B **557**, 147 (2003)
4. G. Abbiendi et al. (OPAL Collaboration), Eur. Phys. J. C **19**, 229 (2001)
5. P. Achard et al. (L3 Collaboration), Eur. Phys. J. C **40**, 333 (2005)
6. M. Bilenky et al., Nucl. Phys. B **409**, 22 (1993)
7. P. Aarnio et al. (DELPHI Collaboration), Nucl. Instrum. Methods A **303**, 233 (1991)
8. P. Abreu et al. (DELPHI Collaboration), Nucl. Instrum. Methods A **378**, 57 (1996)
9. J. Abdallah et al. (DELPHI Collaboration), Eur. Phys. J. C **34**, 127 (2004)
10. A. Ballestrero, R. Chierici, F. Cossutti, E. Migliore, Comput. Phys. Commun. **152**, 175 (2003)
11. E. Accomando, A. Ballestrero, Comput. Phys. Commun. **99**, 270 (1997)
12. E. Accomando, A. Ballestrero, E. Maina, Comput. Phys. Commun. **150**, 166 (2003)
13. S. Jadach, B.F.L. Ward, Z. Was, Comput. Phys. Commun. **130**, 260 (2000)
14. T. Sjöstrand, PYTHIA 5.719/JETSET 7.4, *Physics at LEP2*, ed. by G. Altarelli, T. Sjöstrand, F. Zwirner, CERN 96-01, vol. 2 (1996), p. 41
15. T. Sjöstrand et al., Comput. Phys. Commun. **135**, 238 (2001)
16. G. Gounaris et al., Int. J. Mod. Phys. A **8**, 3285 (1993)
17. J. Abdallah et al. (DELPHI Collaboration), Eur. Phys. J. C **46**, 295 (2006)
18. J. Abdallah et al. (DELPHI Collaboration), Eur. Phys. J. C **55**, 1 (2008)
19. CERN-PH-EP/2008-020 and arXiv:0811.4682 [hep-ex], November 2008